




3D Simulations and MLT. I. Renzini's Critique

W. David Arnett¹ , Casey Meakin^{1,2,3}, Raphael Hirschi^{4,5}, Andrea Cristini^{4,6}, Cyril Georgy⁷, Simon Campbell⁸, Laura J. A. Scott⁴, Etienne A. Kaiser⁴, Maxime Viallet¹, and Miroslav Mocák¹

¹ Steward Observatory, University of Arizona, 933 N. Cherry Avenue, Tucson AZ 85721, USA; wdamett@gmail.com

² Karagozian & Case Inc., Glendale, CA 91203, USA

³ Meakin Technologies, Pasadena, CA 91104

⁴ Astrophysics Group, Keele University, Lennard-Jones Laboratories, Keele, ST5 5BG, UK

⁵ Kavli IPMU (WPI), The University of Tokyo, Kashiwa, Chiba 277 8583, Japan

⁶ Department of Physics and Astronomy, University of Oklahoma, Norman, OK 73019, USA

⁷ Department of Astronomy, University of Geneva, Ch. Maillettes 51, 1290 Versoix, Switzerland

⁸ Monash Centre for Astrophysics, School of Physics and Astronomy, Monash University, Clayton 3800, Australia

Received 2018 October 5; revised 2019 April 24; accepted 2019 May 14; published 2019 August 27

Abstract

Renzini wrote an influential critique of “overshooting” in mixing-length theory (MLT), as used in stellar evolution codes, and concluded that three-dimensional fluid dynamical simulations were needed. Such simulations are now well tested. Implicit large eddy simulations connect large-scale stellar flow to a turbulent cascade at the grid scale, and allow the simulation of turbulent boundary layers, with essentially no assumptions regarding flow except the number of computational cells. Buoyant driving balances turbulent dissipation for weak stratification, as in MLT, but with the dissipation length replacing the mixing length. The turbulent kinetic energy in our computational domain shows steady pulses after 30 turnovers, with no discernible diminution; these are caused by the necessary lag in turbulent dissipation behind acceleration. Interactions between coherent turbulent structures give multi-modal behavior, which drives intermittency and fluctuations. These cause mixing, which may justify use of the instability criterion of Schwarzschild rather than the Ledoux. Chaotic shear flow of turning material at convective boundaries causes instabilities that generate waves and sculpt the composition gradients and boundary layer structures. The flow is not anelastic; wave generation is necessary at boundaries. A self-consistent approach to boundary layers can remove the need for ad hoc procedures of “convective overshooting” and “semi-convection.” In Paper II, we quantify the adequacy of our numerical resolution in a novel way, determine the length scale of dissipation—the “mixing length”—without astronomical calibration, quantify agreement with the four-fifths law of Kolmogorov for weak stratification, and deal with strong stratification.

Key words: convection – stars: interiors – turbulence

1. Introduction

The standard treatment of convection in stellar evolution theory is “mixing-length theory” (Böhm-Vitense 1958, MLT), which uses a semi-empirical, “engineering” approach, based upon an approximate model due to Prandtl (Prandtl 1925; also Clayton 1968; Kippenhahn & Weigert 1990; Hansen et al. 2004). It is local, requires calibration, and has little connection to modern methods used by the turbulence community (e.g., Pope 2000; Davidson 2004).


The main sites of convection in stars are (1) thermonuclear burning zones (with depths of a few pressure scale heights or less), (2) stellar envelopes (with depths often of 20 pressure scale heights or more), and (3) stellar atmospheres, which are also highly stratified, but in addition have dynamically important magnetic fields and require the radiative transfer (rather than radiative diffusion) to describe photon escape. Burning occurs in or near the hottest regions (the cores), where density gradients tend to be small, while envelopes occur near the coolest regions, where density gradients are large, and atmospheres at stellar surfaces, where density gradients are also large. The simpler case, convection in weak stratification, is relevant to burning shells and cores, which have composition gradients. Strong

stratification will be dealt within Paper II. As we will show, MLT, which has zero net flux of kinetic energy, is a weak stratification theory and ignores composition gradients.

Since its introduction, many attempts to improve MLT have been made (Spiegel 1971, 1972), involving many issues such as non-locality, turbulence, and time dependence (e.g., Gough 1967; Unno 1967; Arnett 1968; Kufuss 1986; Xiong 1986; Canuto & Mazzitelli 1991; Canuto 2012a). Despite these efforts, and the widespread conviction that MLT needs improvement, some version of the original MLT is at the heart of almost all modern stellar evolutionary codes.

We consider numerical simulations of the classic Böhm-Vitense problem, which is standard for stellar evolution and interiors, thus avoiding complications such as atmospheres, rotation, and magnetic fields. We do consider turbulence, wave generation, composition gradients, and boundary physics, which were not part of the original Böhm-Vitense solution,⁹ but should have been.

In Section 2 we summarize Renzini's critique of the misuse of MLT. In Section 3 we discuss computational results for flows and formation of boundary layers, while in Section 4 we show behavior of the turbulent kinetic energy (TKE), including multi-

 Original content from this work may be used under the terms of the [Creative Commons Attribution 3.0 licence](https://creativecommons.org/licenses/by/3.0/). Any further distribution of this work must maintain attribution to the author(s) and the title of the work, journal citation and DOI.

⁹ We avoid the terminology shallow and deep for stratified convection in stars, which may seem to be reversed in the stellar case. Weak stratification tends to occur deep in the central regions of stars (which typically contain a few pressure scale heights), while convection at or near stellar surfaces is highly stratified (often ~ 20 pressure scale heights).

modal behavior and wave generation. In Section 5 we present implications of computational results in Section 3 and Section 4, including those for non-analytic behavior at boundaries, and how that may be removed by analytic continuation and wave generation. In Section 6 we discuss composition gradients and boundary layer structure. In Section 7 we summarize this paper and indicate extensions to be found in Paper II (Arnett et al. 2019).

2. Renzini’s Critique

It is appropriate here to warn the reader that two assumptions of MLT already are violated by the 3D simulations: (1) the turbulent velocity field is nonlocal, and (2) the net radial TKE flux is not always negligible.

2.1. The “Embarrassments”

To guide our discussion of MLT, we use the critique by Renzini (1987), who focused on convective “overshooting,” a term that denotes attempts to deal with boundaries in a merely local theory. In discussing some proposed overshooting algorithms, Renzini identified several fundamental problems with MLT that he labeled as “embarrassing”:

1. The ends problem: infinite accelerations and decelerations are required at the beginning and end of the MLT trajectory. MLT does not define a boundary, so that additional physics must be assumed, usually involving the Schwarzschild or the Ledoux linear stability condition.
2. The two lengths problem: are the path length and the size of the “blob” the same?
3. The resolution problem: are lengths resolved which are smaller than the mixing length ℓ (or a pressure scale height H_p)? Is a convective cell of the order of the zone size?
4. The fluctuations problem: turbulent fluctuations are ignored even if not small, so that MLT does not deal with a “storm of the century” event, nor the accumulated effects of fluctuations.
5. The origin problem: what is the flow pattern near the center of the star? Conservation of baryons requires that any flow into the central regions must be balanced by a flow out; if the radial velocity is nonzero at the origin, then its gradient must be zero.
6. The braking problem: what causes the flow to turn and be contained in the convection zone? This requires buoyancy braking, which is not in MLT, and is often patched by “overshoot” prescriptions.
7. The dynamics problem: Renzini’s “wind and waterline” problem, or “boundary layer” dynamics. How are waves generated? How do convective boundaries grow and recede?
8. The non-locality problem: what are the turbulent trajectories, and do distant regions affect local motion?
9. The flux of TKE problem: this is ignored in MLT but has been demonstrated to be non-negligible for strongly stratified flows (e.g., surface convection zones in stars).
10. The composition problem: composition is assumed to be homogeneous in MLT, which is violated in regions having nuclear burning or element diffusion, for example.

Basing our analysis on 3D simulations, which involve minimal assumptions for this problem, we focus on the

question: why does MLT work at all, and what is still missing? It has become traditional to complain about the flaws of MLT, but as Renzini (1987) emphasized, MLT works surprisingly well in some respects.

3. Simulation Methods

3.1. Navier–Stokes Finite Differences and Artificial Viscosity

Early 3D simulations of stellar convection involved stellar atmospheres (e.g., Atroshchenko & Gadun 1994; Asplund et al. 1999), their focus being on the formation of stellar spectra. Following the pioneering work of Nordlund and Stein, Nordlund et al. (2009) performed an extensive series of implicit large eddy simulations (ILES) by the STAGGER code, which uses hyperviscosity to stabilize the hydrodynamic equations and did not include the lower boundary of the convection zone. Composition homogeneity was assumed.

The hyperviscosity method is a descendant of the pseudo-viscosity method (von Neumann & Richtmeyer 1950) for capturing shocks. High frequency motions are strongly damped by a chosen numerical viscosity (much larger than true viscosity of stellar plasma), which causes a strong bottleneck in the turbulent velocity spectrum (Haugen & Brandenburg 2004); compare Figure 1 in Haugen & Brandenburg (2006) to Figure 8 in (Cristini et al. 2017). A goal of the method is to move any motion away from a grid boundary, hopefully minimizing the importance of boundary effects. It appears that this method is consistent with our simulations (at least away from our composition gradients and boundaries), but seems to require more zones to attain the same resolution (Sytine et al. 2000; Haugen & Brandenburg 2004, 2006).

In general, higher resolution allows higher effective Reynolds numbers to be simulated, an important issue for stellar interiors that are highly turbulent (Arnett & Meakin 2016).

3.2. Euler Equations and Finite Volumes

We have taken a different approach: we perform numerical simulations of the Böhm-Vitense problem, with no other approximations except those inherent in finite computational power (i.e., spatial resolution; Meakin & Arnett 2007b; Arnett et al. 2009, 2015; Arnett & Meakin 2011; Viallet et al. 2013; Mocák et al. 2014, 2018; Cristini et al. 2017, 2019).

To capture turbulence we use ILES, which have sufficient resolution to be turbulent, are large enough to capture the integral scale of the flow, and extend down to smaller scales that are well inside the turbulent spectrum. We exploit the fact that the turbulent spectrum is determined by its large scales, so that still smaller scales need not be specified explicitly. For a fixed volume, greater spatial resolution implies a higher effective Reynolds number (i.e., more realistic turbulence; discussed later). The simulations extend in resolution from above the integral scale of turbulence, down to well inside the inertial range of the cascade (Cristini et al. 2017); see also Sytine et al. (2000), Grinstein et al. (2007), Woodward (2007), and Arnett et al. (2015). The full cascade is represented because the method used (PPM, Colella & Woodward 1984) solves the Riemann problem for nonlinear flow at the individual zone level. This method and others of its class (finite-volume monotonic solvers; Leveque 2002; Grinstein et al. 2007) automatically result in a description of the turbulent cascade down to a dissipation scale at the grid level.

This happens because these ILES methods use Riemann solvers to capture shocks at the scale of a zone Δr . They relate

the change in TKE $(\Delta v)^2$ and traversal time $\Delta r/\Delta v$ across the shock to the rate of specific entropy production across the shock $-\frac{\partial S}{\partial t} \sim (\Delta v)^3/\Delta r$. This resembles the Kolmogorov expression for a turbulent cascade, so these methods automatically (“implicitly”) match motion to a turbulent cascade at the grid scale.¹⁰ Conservation of mass, momentum, and energy are enforced to machine accuracy, so that numerical error is concentrated in the calculated shape of the flow field, not the conservation laws. Turbulent kinetic energy is “fed into a smaller scale of the cascade” at the grid level. At larger scales, the cascade is directly computed. Fluctuations at the grid scale are treated as Riemann discontinuities. No explicit model for “sub-grid turbulence” is needed; only a Riemann solution at the grid level, which the shock-capturing algorithm provides automatically. Kolmogorov theory is not an added constraint, but simply an approximation to the numerical result of the conservation laws; see further discussion of Kolmogorov’s four-fifth’s law in Frisch (1995) and Paper II.

These simulations solve the Euler equations (with Riemann boundary conditions), not the Navier–Stokes equations with explicit viscosity, so the question of turbulent instability is determined by the effective Reynolds number. The formal Rayleigh number may be infinity (no explicit radiative diffusion¹¹ for cases dominated by neutrino cooling). The 1D model used for guidance (Cristini et al. 2017) had a very high Péclet number ($Pe \sim 10^8$), but the turbulent cascade implies that the results are insensitive to Pe (see also Orvendahl et al. 2018). The convective Mach numbers are small (<0.02).

For these simulations, the effective Reynolds numbers are roughly $Re \sim (n/2)^{4/3}$, where $n/2$ is the number of zones across the turbulent domain in an n^3 simulation. With $n = 128$ to 1536, Re is ~ 256 to more than 7×10^3 . This allows us to compute from the integral scale of fully turbulent flow, down into the inertial range of the cascade,¹² with no additional assumptions concerning flow geometry.

The ILES approach is a natural complement to the more traditional Direct Numerical Simulation (DNS), which resolves the dissipation scale (Pope 2000) but generally cannot deal with turbulence at those scales that generate motion in stars. In contrast, ILES resolves these large scales, but approximates (by a cascade) the behavior downward to a much smaller dissipation scale. DNS and ILES have different strengths and weaknesses, so that taken together they provide a fuller picture.

3.3. Methods: ILES and Reynolds Averaging (RA)

To tame the turbulent fluctuations, we integrate over the angle (or the horizontal dimension of the convective region), and over several turnover times, to obtain the average behavior over a spherical shell. A novel and key feature of our procedure is that it avoids the classical closure problem of the Reynolds-averaged Navier–Stokes (RANS) equations (Tritton 1998). Also, the numerical simulations do not have the unphysical

¹⁰ See Chapter 2 in Grinstein et al. (2007), and Section 4 in Paper II, Arnett et al. (2019).

¹¹ Some simulations had realistic radiative diffusion added, but it was too small to have a noticeable effect on the neutrino cooled cases. For the cases dominated by radiative cooling, radiative diffusion was obviously important, but the boundary composition profile seems to remain the same, perhaps due to the stronger effects of turbulence; see Section 6.

¹² We explicitly confirm that this range is attained, using both turbulent velocity spectra (Figure 8, Cristini et al. 2017), and dissipation rates (see Paper II).

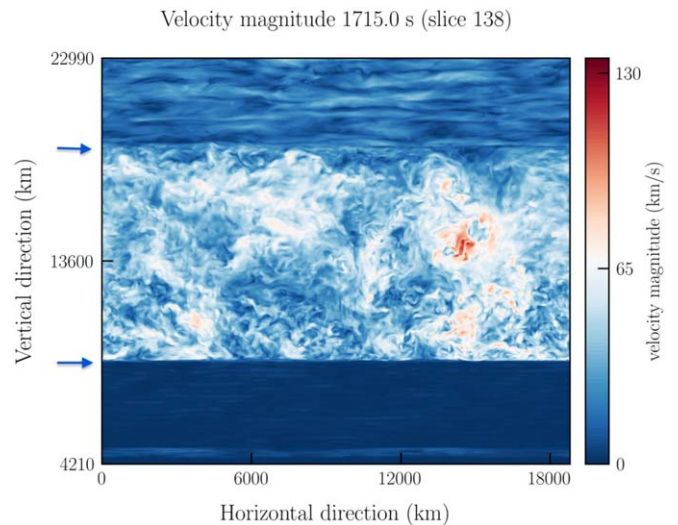


Figure 1. Vertical slice of a 3D, 1024^3 simulation of a carbon-burning shell (Cristini et al. 2017). The energy generation rate is scaled by 10^3 so the Mach number for convection is $Ma \sim 10^{-2}$. The convective region comprises about three pressure scale heights. We estimate the numerical Reynolds number to be $Re \sim 4 \times 10^3$. Velocity magnitudes are shown (red is high; white is medium; blue is low). This figure illustrates the complexity of the turbulent flow, which fills the volume available, and strikingly shows the boundary layers (blue arrows) which form at top and bottom of the convective region. The structures—rolls and plumes—are intermittent: forming, breaking apart, and re-forming elsewhere. Thin boundary layers (horizontal arrows) form naturally as surfaces of separation between turbulent and potential flow; they are dynamic and radiate waves (gravity waves are most clearly visible at the top).

non-dynamic fluctuations found in unconstrained statistical methods, and therefore provide exact averages, limited only by the granularity of the spacetime grid. To be precise, we call our method “Reynolds-Averaged ILES,” or RA-ILES (Mocák et al. 2018). The RA-ILES method allows an accurate and separate assessment of dissipation due to (1) turbulence and (2) resolution error, as we show in Paper II. A comparison of simulations with different resolution shows the effects of finite zoning.

3.4. Numerical Results

Our numerical method uses microphysics (equation of state for stellar matter, reaction networks, neutrino emissivities, and radiative opacities) comparable to current usage in stellar evolution codes. Composition gradients and boundaries are calculated in detail.

Our method has internal tests of numerical resolution, which we examine in detail in Paper II (Arnett et al. 2019). These tests suggest that at our highest spatial resolution, the errors from finite cell size are already small, even in the challenging lower turbulent boundary.

Our set of 3D numerical simulations¹³ are “box-in-star” computations that range from “very low resolution” (128^3 zones) to “very high resolution” (now 1536×1028^2 and 1536^3 zones). These are ILES; see Grinstein et al. (2007), Woodward (2007), Apsden et al. (2008). They include two stable layers sandwiching a turbulent convective region; see Figure 1, which shows a cross-sectional slice through a representative case.

¹³ See Meakin & Arnett (2007b); Arnett et al. (2009, 2015); Arnett & Meakin (2011); Viallet et al. (2011); Cristini et al. (2017, 2019); Mocák et al. (2018); C. Georgy et al. 2019, in preparation.

Velocity magnitudes are shown (red is high; white is moderate; blue is low). This figure illustrates the complexity of the turbulent flow and strikingly shows the boundary layers that form along the top and bottom of the turbulence. The boundary layers are thin and not step functions but sigmoids (Arnett & Moravveji 2017; Cristini et al. 2017). Coherent structures—rolls and plumes—are strongly dynamic: forming, breaking apart, and re-forming elsewhere. Both boundary layers are also dynamic. They bend and stretch, and radiate gravity waves (which are most clearly visible at the top). There is intermittency (Tennekes & Lumley 1972) in both space and time, as the “patchiness” in Figure 1 indicates; intermittency is related to nonlinear interactions of coherent structures (Warhaft 2002).

This is confirmed by movies of (1) the evolution in time (“Very high resolution movie of the C shell”) and (2) a fly-through of the computations at a given instant in time (“Carbon shell [1024³] simulation: fly-through movie”).¹⁴ To the extent that the simulations are in a statistical steady state in time, and statistically homogeneous in space, the movies will have a similar visual appearance (as they do here). This allows averaging procedures to be robust.

3.5. Kolmogorov and Intermittency

ILES methods were initially considered as an alternative to sub-grid methods (SGS) in that a sub-grid model is replaced by a turbulent cascade (see Section 3.2; Grinstein et al. 2007). Kolmogorov theory is one of the success stories of turbulence (Frisch 1995), but it too is not perfect, as it does not contain the direct influence of the large scales on small scales (Warhaft 2002) and the phenomena of intermittency (Tennekes & Lumley 1972). We were pleased to find that our simulations naturally develop intermittency and a turbulent velocity spectrum resembling Kolmogorov (see Paper II; Cristini et al. 2019); these are not imposed. This is accomplished at least in part by the nonlinear interaction of large-scale coherent structures (multi-modes, Figure 2), with regions of large time dependency (waves), giving intermittency (Tennekes & Lumley 1972; Holmes et al. 1996, Section 3).

3.6. Limitations: Rotation and Magnetohydrodynamic (MHD)

Even a perfect solution to the Böhm-Vitense problem would not solve the more general issue of convection in stars.

Featherstone & Hindman (2016) suggest that supergranulation is a rotationally constrained flow; to add rotation goes beyond the Böhm-Vitense formulation. Rotation requires a star-in-box approach to capture the largest scale (Porter & Woodward 2000). Rotation forces non-locality (Arnett & Meakin 2010) and symmetry breaking (Viallet et al. 2013).

To the extent that MHD is important, symmetry is broken again. This symmetry is that upon which Kolmogorov and we rely; this problem is an issue for future research.¹⁵ Turbulence makes and stretches vortices (e.g., Pope 2000); a seed magnetic field will be compressed (doing work against magnetic pressure) and stretched (doing work against magnetic

tension; see Parker 1979; Davidson 2001). Fluid kinetic energy is therefore converted into magnetic field energy, and fluid flow is retarded, giving a dynamo. Magnetic fields are buoyant and will rise in a gravitational field. Unless all the field escapes, it strengthens. Stronger magnetic fields tend to stop the flow, which then no longer generates magnetic field, allowing convection to reassert itself. There is a tendency for a magnetic cycle, reminiscent of the solar cycle.

Stars are made of high energy-density plasma,¹⁶ so that magnetic fields will be ubiquitous in stars, but what geometry, strength, and dynamic behavior will they have? Geometry is evidently important: 2D turbulent flow develops a reverse cascade in which strong vortices form, merge, and grow in size, while in 3D such vortices are shredded into the extra degrees of freedom.

We have chosen the simplest version of this problem: non-rotating, non-magnetic Böhm-Vitense convection. We have added turbulence, stratification, non-uniform composition, time dependence, non-locality, and boundary physics, but incorporating rotation and magnetic fields remains a challenge for the future.

4. Numerical Evolution of TKE

Kolmogorov dissipation is derived for a homogeneous, isotropic turbulent medium (Frisch 1995), where boundaries are not important. Consequently, we first examine the behavior of specific TKE in bulk, reserving a discussion of boundaries until later (Section 6).

How much kinetic energy is involved in the convective motion? This is Renzini’s flux of TKE problem. Figure 2, top pane, shows the evolution in time of specific TKE in the carbon-burning simulations (Cristini et al. 2017, 2019), for resolutions of 128³, 256³, and 512³. Multi-mode behavior, like that seen in Meakin & Arnett (2007b; Figure 4) and Arnett et al. (2009; Figure 5), is evident. Simulations of 768³, 1024³, and 1536³ were not continued for such long times, but they tracked the 256³ and 512³ results; a short segment of the 1024³ case is shown in cyan. All simulations are consistent with an approach to a quasi-steady state, but with significant and continuing fluctuations around that average value. Such behavior, while typical of turbulent flows, is not in MLT (Renzini’s fluctuation problem), but is a feature of high resolution simulations; see also Figure 5 in Woodward et al. (2015).

4.1. Initial Transient

Each simulation is initiated from a hydrostatic state, recalculated on the grid to machine accuracy. It is then overlaid with very small random perturbations in density, with amplitudes that were 10⁻³ of the initial static density. Convection grows gently in the unstable region, forming a nonlinear chaotic flow (the turbulent cascade plus coherent structures). The convective Mach numbers rise to ~10⁻²; these kinetic energies are 10⁴ times larger than implied by the initial seeds. Such small perturbations quickly disappear in the stable regions.¹⁷

¹⁴ The time evolution and the fly-through movies may be found at <http://www.astro.keele.ac.uk/shyne/321D/convection-and-convective-boundary-mixing/visualisations>.

¹⁵ A preliminary step (Arnett & Meakin 2010) suggests that mild rotation causes turbulent flow to tend toward conservation of specific angular momentum, with dissipation provided by the turbulent cascade.

¹⁶ See Tzeferacos et al. (2018) for a recent experimental attempt on the Omega laser to address this problem.

¹⁷ For the C+C shell simulations, the perturbations were only put in the convective layer. In the O+O simulations, the perturbations were put in stable layers too but quickly disappear from these regions.

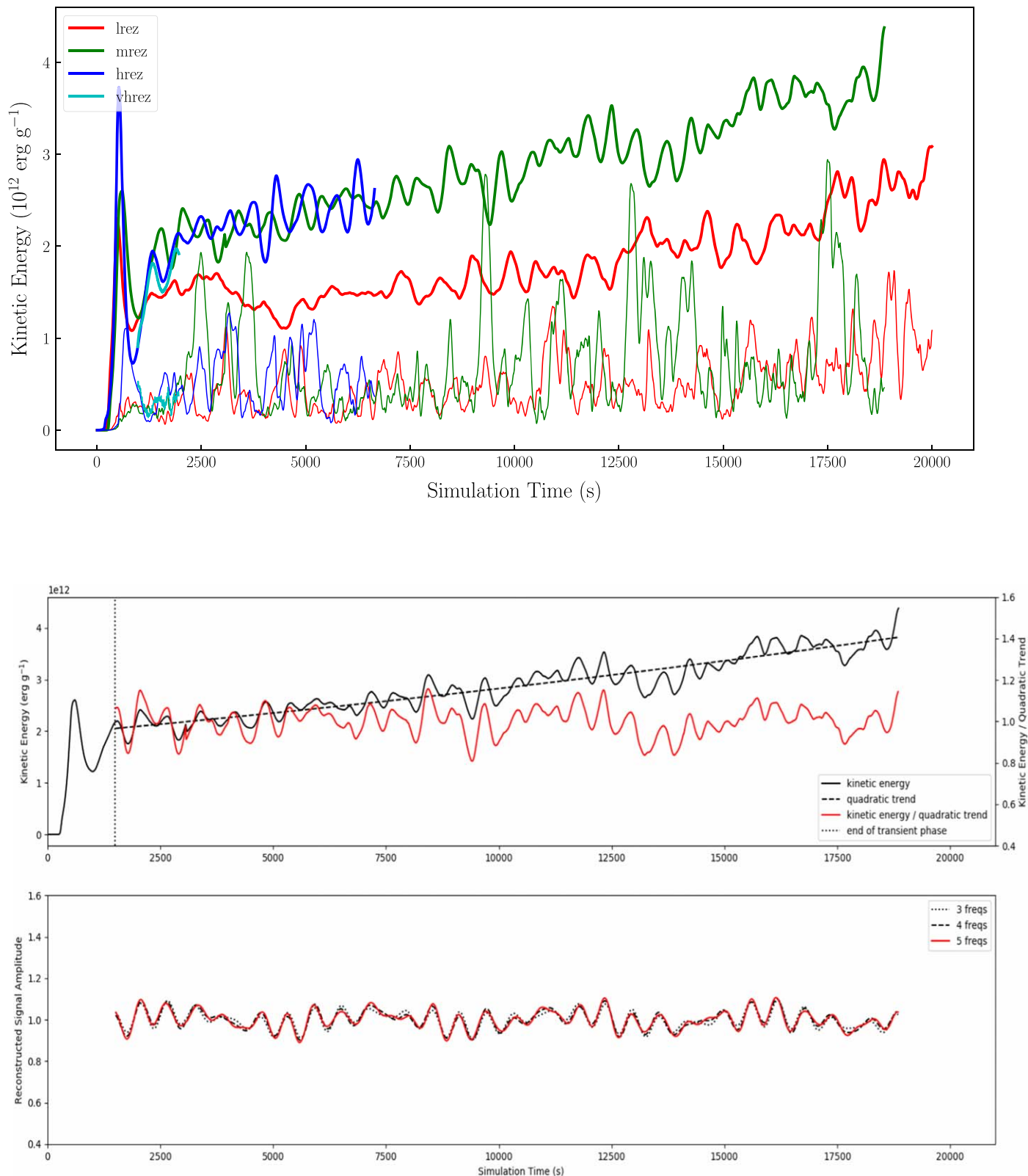


Figure 2. Top panel: specific turbulent kinetic energy (TKE) for the carbon-burning shell (Cristini et al. 2017, 2019) versus radius for 18,000 s. This shows “lrez” (128^3 , red), “mrez” (256^3 , green), “hrez” (512^3 , blue), and “vhrez” (1024^3 , cyan) simulations. Fluctuations in TKE are seen, as found by Meakin & Arnett (2007b). Multi-mode behavior is evident. The 128^3 simulation shows effects of lower resolution (higher numerical viscosity), but 256^3 and 512^3 seem unaffected. Wave kinetic energy (same colors but thin lines) is much smaller and is plotted (multiplied by a factor of 25) along the bottom. Higher resolution simulations (768^3 , 1024^3 , and 1536^3) have not been done for such long times, but agree fairly well with the 256^3 and 512^3 cases. Bottom two panels: mode analysis of 256^3 simulation, for frequencies 1.6, 0.23, 1.8, 0.81, and 2.1 mHz. A trend of $(5.26 \times 10^3 t^2 - 4.41 \times 10^7 t + 1.56 \times 10^{12})$, t in s, was divided out; it corresponds to an evolutionary change (see text). While the pulses are not sine waves, they are periodic, so we separate out a few (five) frequencies that are shorter than the turnover time, as expected for a turbulent cascade. Even five modes begin to capture the “pulses” moderately well (bottom panel). These low order, multi-mode fluctuations are robust features of the TKE; see Holmes et al. (1996).

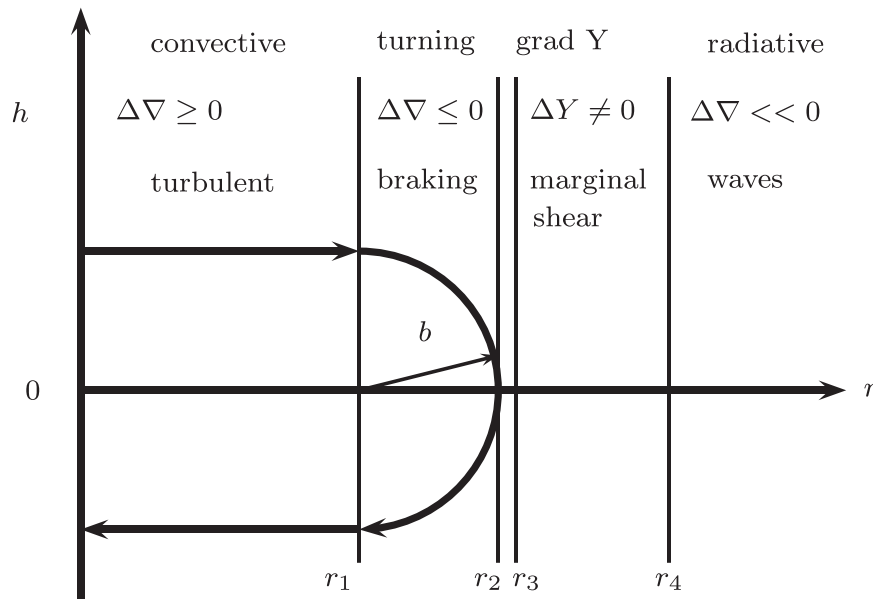


Figure 3. Two-dimensional schematic of the average structure of an upper convective boundary. The length b corresponds to the radius of curvature needed to reverse (contain) the flow ($v_r \rightarrow -v_r$). The centrifugal acceleration is provided by negative buoyancy. The radial direction is denoted by r and the transverse by h . The boundary layer lies between r_2 and r_3 . Imagine the whole system undulating due to turbulent fluctuations.

4.2. Multi-modal Behavior

Initially there is no turbulent dissipation, only driving by buoyancy. A large first pulse develops due to this delay in the turbulent cascade.¹⁸ After this pulse, driving balances dissipation on average, but not exactly: there is a phase lag (Arnett & Meakin 2011), so that the pulses do not disappear because damping always lags driving.¹⁹

There is an evolutionary growth in TKE due to a slight mismatch of thermal balance between initial conditions based on a 1D MLT model and the energetically scaled 3D model (Cristini et al. 2017). The heating was 10^3 of its realistic value; although it hastened the evolution correspondingly, the heating per turnover is still very small in comparison to the internal energy. This enhanced the slow evolutionary rise, both for efficiency in computation and for visibility in the figure. This trend is shown as a line in the middle pane and is removed in order to extract frequencies of the dominant modes (bottom panes). A few (five) modes are sufficient to capture most of the multi-mode behavior, as suggested by Holmes et al. (1996).

Movies of the simulations support the view that the fluctuations in Figure 2 are caused by turbulent break-up of multiple 3D rolls. Such multi-modal behavior also causes motion of the convective boundaries, driving waves into neighboring regions and causing variations in TKE. These pulses are clearly seen in Figure 2 and do not attenuate noticeably over ~ 30 turnover times. There is no evidence that the pulses are transient.

Oxygen burning required no scaling of the heating rate so the consumption of fuel was explicitly followed. However, the interaction of turbulence, burning, and mixing of Ne and O is

¹⁸ Because the first pulse also depends on interactions between multiple modes of flow, there is no guarantee of simple behavior. However, compare Figure 2 to the similar Figure 5 in Woodward et al. (2015), which represents apparently different physics: H entrainment at the top of He-shell flash.

¹⁹ This computational domain was chosen to study separate convective cells; an average over a larger domain (e.g., 4π steradians) would contain more chaotic cells, and might not resolve the pulse behavior so well (Arnett & Meakin 2011), but it still appears (Jones et al. 2017).

more complex than generally realized (Mocák et al. 2018), so that we simplify at this point by focusing on C burning, which is similar but has no Ne ingestion. On these timescales (2×10^4 s), little carbon is consumed, even with the enhanced rate.

The middle pane in Figure 2 shows the original TKE curve and a flatter one after “detrending” to remove the effect of a slow thermal evolution (see caption). The bottom pane shows the reconstruction for 5 frequencies, which resembles the “detrended” curve; at 10 frequencies (not shown) the fit is excellent, but even a few modes are sufficient to capture the basic behavior. A proper orthogonal decomposition should allow a better representation (Holmes et al. 1996), but for now we simply want to emphasize the robust nature of the pulses in time and across different simulation resolutions. The pulses, which are comparable to a transit time in duration, imply that statistical estimates of turbulent properties will be modulated by multi-mode behavior, unless averaged over many transit times.

Figure 2 illustrates the problem for stellar evolution: how do we integrate over the pluses in TKE (the weather) without losing the slower evolution of the “detrending curve” (the climate)? In Section 5 and the Appendix, we will (1) separate the velocity field into a 3D turbulent component \mathbf{u}' , which varies rapidly, and a slowly varying radial velocity U_r of the spherical mass shells of the stellar model; (2) integrate over the rapid variations in time and space of \mathbf{u}' to obtain average properties and second order correlations needed for stellar evolution; and (3) connect these to a stellar evolution framework (321D).

4.3. Resolution

With each new level of spatial resolution, synchronization is lost, so that each simulation is an independent member of an ensemble, all of which are attracted to the cascade in the long term. The RA-ILES integrated values are reproduced with surprising accuracy even at crude resolution (128^3) and are well

resolved at (256^3) and above (Meakin & Arnett 2007b; Viallet et al. 2013; Arnett et al. 2015; Cristini et al. 2017, 2019).

The lowest resolution case (128^3) has the highest numerical dissipation; it settles toward a quasi-steady state with the lowest TKE in Figure 2. This higher dissipation may also be responsible for the reduced amplitude of the TKE peaks in 128^3 relative to, for example, the 256^3 simulation. While high resolution and long evolution are both desirable, they are in conflict for a finite computer budget, so the highest resolution runs are relatively short.

4.4. Linear Stability Theory

Figure 2 contains another implication for stellar physics. In linear stability theory (Unno et al. 1989; Aerts et al. 2010), it is not possible to include a realistic treatment of convective driving and damping because these terms are inherently nonlocal and nonlinear (see discussion of the τ -mechanism in Arnett & Meakin 2011). Pulses such as those shown in Figure 2 drive “stochastic” stellar variability.

This issue is sometimes called the “time-dependent convection” problem. Because of intermittency, convection is only “steady state” in an average sense, if at all. Turbulent convection drives waves that, once launched, may then be described by linear theory. A sequence of increasingly stronger waves (increasing convective Mach number) transforms pulsations into explosions (Cristini et al. 2017, 2019).

4.5. Wave Generation

The kinetic energy in waves is shown as thin lines, scaled up by a factor of 25 for better visibility, at the bottom of the top pane in Figure 2. Arnett et al. (2015) showed that the boundary of convection has a particular, dynamically required structure, which implies a particular rate of wave generation. In order for matter to turn and remain in the turbulent zone, outgoing flows must be decelerated. Buoyancy braking requires that the square of the Brunt–Väisälä frequency change sign (Equation (11)), so waves are supported, with their amplitude depending upon the stellar structure and the vigor of convection. The buoyancy braking provides a direct connection between convective and wave motion.

The behavior is complicated by intermittency caused by large-scale waves interacting nonlinearly (e.g., Figure 2, top panel, thin lines).

Thus the physics of a convective boundary requires the generation of waves (see also Section 5.4). It is a complex dynamic problem, involving the chaotic and nonlinear behavior of turbulence, wave motion, and boundary flexing. In this case, the energy in the waves is small relative to that in convective motion, as Figure 1 shows. See also Section 6, Figure 4, where at $r < 0.43 \times 10^9$ cm, the blue curve gives evidence for a background of gravity waves.

5. 321D Analysis

Baryon conservation and the assumption of a quasi-static, quasi-spherical background place strong general constraints on the nature of convective flow in stars.

The simulations in Figure 1 have no net accumulation or deficit of mass due to turbulent motion. In Figure 2 we see a steady pulsing behavior, which recurs on a short timescale, and a much slower evolutionary change. Over an intermediate timescale, the combined space and time average of $\langle \partial_t \rho_i \rangle$ is

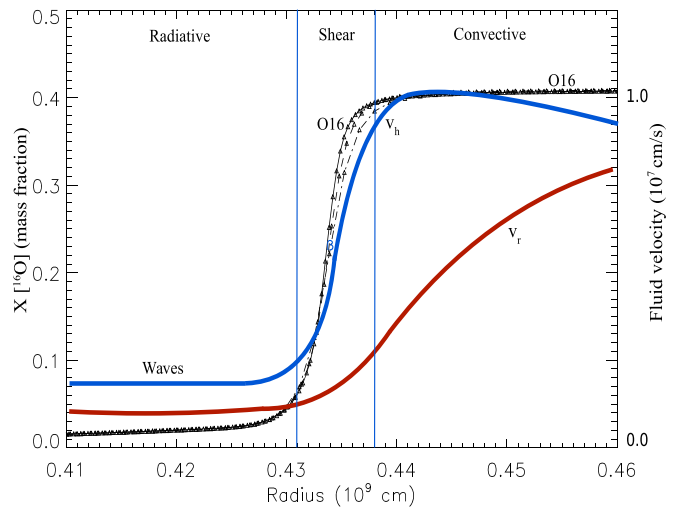


Figure 4. Comparison of the ^{16}O composition profiles (black), at a lower boundary, averaged over angle, for different resolutions (“med-res” [384×256^2 , triangles] and “hi-res” cases [768×512^2 , heavy triangles] of Viallet et al. 2013, and a “very-hi-res” case [1536×1024^2], heavier triangles, the “Perth” simulation; see Arnett et al. 2015), at the bottom boundary (which seems to be approaching numerical convergence; see Paper II, Arnett et al. 2019). This shape has striking similarity to that inferred from asteroseismology (Arnett & Moravveji 2017) for convective cores of red giants. See also discussion of the C+C shell in Cristini et al. (2017, 2019). Overdrawn are the rms velocity profiles averaged over a spherical shell and normalized arbitrarily to fit the graph; red is radial and blue represents the two horizontal directions. Notice the excess of horizontal velocities over radial at the shear boundary, characteristic of turning flow. Instantaneous profiles are not exactly spherical or constant but dynamic. The velocities do not go to zero outside the convective zone ($r < 0.43 \times 10^9$ cm) because of significant but small wave motion (see Figure 1), which was generated in the shear region.

small and slowly varying (true evolution would be at least 10^3 longer; see Section 4), so from baryon conservation, these simulations imply

$$\langle \overline{\nabla \cdot \rho \mathbf{u}'} \rangle \approx 0, \quad (1)$$

where the angle brackets denote an average over a spherical shell, an overline implies an average over a few turnover times, \mathbf{u}' is the vector representation of the 3D velocity fluctuations relative to a 1D spherical, co-moving (Lagrangian) frame, and $\rho = \rho_0 + \rho'$ is the total mass density, including fluctuations, so the equation is nonlinear. Because of the time dependence, compressional waves are supported and may be necessary (although weak, as in Figure 2).

5.1. The Anelastic Approximation of Gough

Although superficially similar,²⁰ Equation (1) differs from the simpler anelastic approximation of Gough (1969),

$$\langle \nabla \cdot \rho \mathbf{u} \rangle = 0, \quad (2)$$

which suppresses compressional waves because the term $\partial_t \rho$ in the continuity equation is set to zero for all times (not just on average). Equation (2) requires homogeneity in composition, weak stratification, and does not deal with compressible effects of turbulence, fluctuations, or boundary dynamics, as does Equation (1).

²⁰ Equation (1) has two averages (angle and time) rather than the one (angle) average seen in Equation (2).

Verhoeven et al. (2015) compare anelastic and compressible simulations, ignoring the effects of composition. Their Figure 2 appears similar to some of our simulations (e.g., Meakin & Arnett 2007a, 2007b) having a numerical Reynolds number of $Re \sim 650$ to 10^3 or so. As they point out, unfolding such parameters from different computational methods is difficult, so our estimate is only suggestive. This might explain why our simulations in Figures 1 and 2 seem more turbulent than theirs. A second point of difference is their treatment of boundaries. They have no stable layer (above or below) on their grid, and there is no indication of a boundary layer or wave radiation.

Brown et al. (2012) analyze why some formulations of anelastic approximations exhibit failures of energy conservation; we have avoided imposing anelasticity (“sound proofing”) so we could maintain strict obedience to conservation laws. See also (Gough 1969), whose original formulation avoided the energy non-conservation problem.

Our simulations use the complete fluid-dynamic equations and are sufficiently general to have produced consistency with Equation (2), but preferred Equation (1) instead. In our simulations, sound waves are merely weak (Equation (1)), not zero (Equation (2)). This weakness (see Figure 2) is associated with the low Mach number of the flow, not an imposed mathematical condition.

In our simulations, compressional waves may be necessary for convective boundary conditions and boundary layers, as breaking water waves and shock waves need thin layers of high dissipation; see Section 5.4.1.

5.2. Stratification and Length Scales

Averages are necessary to deal with the significant fluctuations due to turbulence. Equation (1) is more general than Equation (2); it allows solutions, which violate Equation (2) for part of a cycle, but cancel this error for the remainder, maintaining the average (i.e., compressional waves).

A measure of stratification is the density scale height, $H_\rho \equiv -(\partial_r \ln \rho_0)^{-1}$, so roughly,

$$\nabla \cdot \mathbf{u}' \approx u'_r / H_\rho. \quad (3)$$

The simulations support Equation (3) as an approximation which connects the structure of 3D convective velocity fluctuations \mathbf{u}' to a length scale of stratification without any explicit MLT assumption (Viallet et al. 2013).

For uniform density, $H_\rho \rightarrow \infty$. For a medium of weak stratification, the length scale increases to become the size of the convection zone. Viallet et al. (2013), in their Section 4.2.1, have confirmed that these approximations apply to a turbulent stellar medium, for both a red-giant (strongly stratified) and an oxygen burning (weakly stratified) model, and are generally true for low Mach-number convection, as we confirm.

This gives a characteristic length scale for a quasi-steady flow in a stratified medium (such as stellar convection). However, this equation is linear in velocity, so that the velocity scale is not constrained; another equation is required (e.g., involving convective enthalpy flux).

Any form of “rotational” flow (Equation (1)) can remove the ends problem because such flow turns back to remain in a finite volume. Lorenz (1963) showed that the simplest version of such a flow (a 2D convective roll) is an example of deterministic chaos; the flow chaotically flips from clockwise to counterclockwise. In 3D, the angular momentum vector is

not restricted to only two orientations (as in 2D), but may wander through 4π steradians.²¹ Such instabilities associated with one or several strange attractors seem to act as seeds for turbulence (see Section 5 and Arnett & Meakin 2011).

5.3. Turbulent Acceleration Terms

In Appendix A we show how to transform from an Eulerian coordinate system appropriate to 3D simulations to a co-moving 1D system appropriate to stars. We now develop “321D” equations, which capture some of the 3D behavior, for use in a stellar evolution code.

In Appendix B we derive from the Navier–Stokes (or, for ILES, the Euler) equations an expression that connects average rate for dissipation of TKE ϵ_K , with turbulent driving by buoyancy and pressure dilation, minus the divergence of acoustic flux:

$$\begin{aligned} \langle \rho \epsilon_K \rangle &= \langle \rho' \mathbf{u}' \cdot \mathbf{g} \rangle + \langle P' \nabla \cdot \mathbf{u}' \rangle - \langle \nabla \cdot (P' \mathbf{u}') \rangle, \\ &= \mathcal{B} + \mathcal{P} + \mathcal{A} \end{aligned} \quad (4)$$

which is confirmed by ILES (Viallet et al. 2013). The three terms on the right-hand side (rhs) are “buoyancy power” \mathcal{B} , “pressure dilatation” \mathcal{P} , and “divergence of acoustic flux” \mathcal{A} .

MLT is a weak stratification theory and as such uses only the buoyancy power term \mathcal{B} from Equation (4). In MLT, the TKE production is best understood as due to the “buoyancy power” term,²² which is directly related to the enthalpy flux (Arnett et al. 2009). Strong stratification requires pressure dilatation \mathcal{P} as well; see Paper II. Although missing in MLT, waves are produced by any turbulent 3D simulation that is general enough to support them (e.g., Meakin & Arnett 2007b; see Figures 1 and 2).

5.4. Weak Stratification: Balance between Driving and Damping

The chaotic driving of turbulence causes large fluctuations and requires that we average instantaneous properties to obtain useful variables for stellar evolution; see Section 2.6 in Arnett et al. (2015) and Meakin & Arnett (2007b). Fluctuations are not part of MLT; see the fluctuations problem in Section 2. When performed on even modestly resolved numerical simulations of convection, such averaging shows a balance over the turbulent region, between (1) large-scale driving and (2) dissipation at the small-scale end of the turbulent cascade.

For weakly stratified convection zones (and MLT), the buoyancy driving (the work done by buoyant acceleration \mathcal{B} acting on the turbulent velocity fluctuation \mathbf{u}') is

$$\langle \mathbf{u}' \cdot \mathcal{B} \rangle = \overline{\langle \rho' \mathbf{u}' \cdot \mathbf{g} \rangle} \approx u'_r g \beta_T \Delta \nabla, \quad (5)$$

where the gravitational acceleration vector is \mathbf{g} , the super-adiabatic excess is $\Delta \nabla = \nabla - \nabla_e$, and β_T is the thermal expansion coefficient (Kippenhahn & Weigert 1990). The entropy excess $\Delta \nabla$ may contain contributions from composition differences, which are ignored in MLT. To evaluate these, the problem of mixing must be solved consistently with that of

²¹ See Arnett & Meakin (2011) for a roll model, and also Gabriel & Belkacem (2018) for a plume model.

²² Mass conservation used alone causes the buoyancy term to be canceled (e.g., Nordlund et al. 2009), but the combined constraint of hydrostatic equilibrium causes it to reappear (Arnett & Meakin 2011).

convection, complicating the problem (Arnett et al. 2015; Woodward et al. 2015; Mocák et al. 2018).

The rate of dissipation for TKE due to the turbulent cascade is, on average,

$$\overline{\mathbf{u}' \cdot \mathcal{D}} \approx \epsilon_K, \quad (6)$$

which is essentially the Kolmogorov value for homogeneous isotropic turbulence.²³ This is both a theoretical prediction (Kolmogorov 1962) and, independently, a numerical result (Section 3; Meakin & Arnett 2007b; Arnett et al. 2009).

For weak stratification, our RA-ILES numerical simulations (Arnett et al. 2009; Arnett & Meakin 2011) satisfy a local balance on average, between acceleration and deceleration,

$$\overline{\mathcal{B}} \approx \overline{\mathcal{D}}, \quad (7)$$

over the convection zone (Meakin & Arnett 2007b; Arnett et al. 2009, 2015). Thus, on average,

$$v^2/\ell_d \approx g\beta_T \Delta\nabla, \quad (8)$$

which is something like MLT (Kippenhahn & Weigert 1990), but here v is a velocity related to Kolmogorov damping. This equation is nonlinear in velocity and therefore can set a velocity scale for Equation (3), but with the well-defined Kolmogorov damping length ℓ_d replacing the adjustable parameter (mixing length).

5.4.1. Avoiding Non-analytic Behavior

Equation (8) has several flaws: (1) it is independent of composition, (2) it is undefined for $\Delta\nabla < 0$ (stable regions), (3) it is local, and (4) it is static. The simulations are free of all these problems. The velocity in Equation (8) is multi-valued,

$$v = \pm \sqrt{\ell_d g\beta_T \Delta\nabla}, \quad (9)$$

and ill-behaved at $\Delta\nabla = 0$ due to the non-analytic nature of the square root (Section 5.11, Whittaker & Watson 1927). This is the algebraic branch point of the square root function, at which v can have multiple values and an undefined derivative. We note that if $v = \sqrt{w}$, then $dv/dw = \frac{1}{2\sqrt{w}}$, which is singular as $w \rightarrow 0$. These features of MLT cause kinks (cusps) in the velocity field at points where the velocity is not differentiable (e.g., infinite acceleration as $\Delta\nabla$ changes sign; see also Section 9 in Gough 1977). We refer to such non-analytic behavior as “singular.”

Such regions may be avoided by analytic continuation using the acceleration equation. Physically this corresponds to the reintroduction of an inertial term (the total time derivative of the velocity). Such singularities also appear in treatment of boundary layers in Prandtl theory (Section 40, Landau & Lifshitz 1959), as the velocity perpendicular to the surface goes to zero. In a star, the motion does not go to zero but becomes wave-like²⁴ (e.g., Section 4.5; Figure 4).

This is related to the phenomenon of separation Landau & Lifshitz (1959), Section 39, and the formation of boundary

layers, whose width is proportional to $1/\sqrt{\text{Re}}$, where Re is the Reynolds number. Our ILES develop narrow boundary layers (see Figure 1), which do become narrower with higher resolution (larger effective Reynolds number). The condition $v = 0$ at a convective boundary in MLT separates potential from rotational flow and should be treated as a boundary layer (Section 40, Landau & Lifshitz 1959). Such boundary layers differ from the classical case studied by Prandtl (Anderson 2005) in that the interface is fluid-fluid, not fluid-solid, and turbulent, not laminar. Non-slip boundaries are not appropriate.

5.4.2. Acceleration Equation

Avoidance of the non-analytic behavior gives (recovers) an acceleration equation (Gough 1967; Arnett 1968) for the turbulent velocity fluctuation \mathbf{u}' to replace Equation (8),

$$\begin{aligned} d\mathbf{u}'/dt &= \partial\mathbf{u}'/\partial t + \mathbf{u}' \cdot \nabla\mathbf{u}' \\ &\approx \mathcal{B} - \mathcal{D}, \end{aligned} \quad (10)$$

whose solutions may be related to the simulation results for weak stratification. The addition of the inertial term $d\mathbf{u}'/dt$ avoids the singularity at the boundary as intended, at the price of requiring wave generation at turbulent boundaries; even if weak, waves are required for reasonable behavior of the acceleration variable, as well as energy conservation. Equation (10) is basically a statement of Newtonian mechanics, with driving by buoyancy and damping by drag.

Equation (10) applies to wave regions too, where the convective drag term \mathcal{D} is negligible, as it is in wave domains of stars and our simulations. The Brunt–Väisälä frequency squared is

$$\begin{aligned} \mathcal{N}^2 &= g[(d \ln P/dr)/\Gamma_1 - d \ln \rho/dr] \\ &\approx -g\beta_T \Delta\nabla/H_p = \mathcal{B}/H_p \end{aligned} \quad (11)$$

(Aerts et al. 2010, Equation (3.73) for the first expression, and Kippenhahn & Weigert 1990, Equation (6.18) for the second). Here the adiabatic exponent is $\Gamma_1 \equiv (\partial \ln P/\partial \ln \rho)_S$. The second expression requires the assumption²⁵ that the composition gradient is zero (composition homogeneity), using the Schwarzschild discriminant $\Delta\nabla$. Chapter 6 gives an example of the general case (see also Meakin & Arnett 2007b; Cristini et al. 2017; Mocák et al. 2018).

For $-H_p N^2 < 0$ we have wave motion, while for $-H_p N^2 > 0$ we have convective flow that is turbulent.

Gough (1977) gives a historical context going back to Prandtl and to Biermann. The early attempts (and most of the recent ones) have used a kinetic theory of “blobs” model, in which the mixing length was a sort of mean free path. To connect with numerical results, we prefer a model using the momentum equation from fluid dynamics, involving structures such as waves, convective rolls, or plumes (see Figure 1).

²³ The idea of homogeneous isotropic turbulence may be oversimplified. Intermittency and anisotropy observed at small scales may require refinement of the basic Kolmogorov theory (Warhaft 2002); the ILES do provide evidence for these changes. See Section 3.3; Frisch (1995).

²⁴ If the Mach numbers are low, gravity (g -) modes dominate over compressional (p -) modes outside the boundary layer.

²⁵ In our simulations, we find that convective mixing is efficient inside the convection zone, but that composition gradients may develop on the non-convective side of boundaries. However, see the ingestion of a Ne plume in Mocák et al. (2018). Milder convection, and slower burning stages (e.g., H and He) also may be different.

5.4.3. Turbulent Kinetic Energy Equation

Taking the dot product of Equation (10) with \mathbf{u}' gives a TKE equation

$$d((\mathbf{u}')^2/2)/dt \approx \mathbf{u}' \cdot \mathbf{g} \beta_T \Delta \nabla - \epsilon_K, \quad (12)$$

which is satisfied by the ILES simulations (Meakin & Arnett 2007b). Formally there is a steady-state solution²⁶ if there is an exact balance between driving and damping, with $\ell_d \equiv \ell_{\text{MLT}}^2/8H_p$ for MLT and $\Delta \nabla > 0$. In Equation (12), negative values of $\Delta \nabla$ are allowed; this permits buoyant deceleration (Arnett et al. 2015).

The flow is relative to the grid of the background stellar evolution model (see Appendix A), so the co-moving (Lagrangian) time derivative of TKE may also be written as

$$d(\mathbf{u}' \cdot \mathbf{u}')/dt = \partial_t(\mathbf{u}' \cdot \mathbf{u}')/2 + \nabla \cdot \mathbf{F}_K, \quad (13)$$

where $\mathbf{F}_K = \rho \mathbf{u}'(\mathbf{u}' \cdot \mathbf{u}')/2$ is a flux of TKE. The generation of a divergence of the kinetic energy flux in this way is robust for dynamic models; it occurred in the RANS approach as well (Meakin & Arnett 2007b). This flux acts to spread locally driven turbulence more evenly over the turbulent region, to be dissipated as Kolmogorov suggested. Equations (12) and (13) together comprise a simple form of the TKE equation (Meakin & Arnett 2007b) for weak stratification.

Use of the turbulent cascade removes the two lengths problem. The damping length is not a size but a measure of the rate of damping due to turbulence. Further, the cascade approximates all scales down to the dissipation scale of Kolmogorov, so that the resolution problem also disappears.

These results are reminiscent of some previous work—for example, Canuto & Mazzitelli (1991), Canuto et al. (1996), who developed a theory of full-spectrum turbulence, and Canuto (2012a, 2012b, 2012c, 2012d, 2012e), who made further progress with a Reynolds-stress approach. These earlier suggestions, like the 3D numerical simulations, shift the focus from the original MLT picture of blobs to one involving a turbulent cascade.

5.5. A Major Flaw in MLT

MLT has a major flaw, associated with use of Equation (8), which may have biased stellar evolution theorists toward a belief that stellar convection is more placid than it is likely to be. As we saw in Figure 2 (Section 4), phase lags between driving \mathcal{B} and damping \mathcal{D} cause large pulses in TKE (Meakin & Arnett 2007b; Arnett & Meakin 2011). These are ignored in MLT but have been prominent in all of our ILES work.

Stellar convection is better thought of as a “chaotic ensemble of storms,” as ILES shows, rather than a steady, well-behaved flow. Setting $\mathcal{B} = \mathcal{D}$ as a universal condition, instead of an average one, will filter out these large fluctuations, but not account for all their effects. This flaw is related to some of the mixing issues found when using MLT (e.g., in the sdB stars; Schindler et al. 2015).

In order to converge, stellar evolution codes require that such fluctuations be integrated over to get a sufficiently stable, quasi-steady target state. These ILES fluctuations are not negligible. For example, fluctuations in TKE were a prominent

new result of the first 3D simulations of an oxygen burning shell (Meakin & Arnett 2007b). These began from an initial 1D model constructed using the Ledoux criterion, which is the correct choice for linear stability theory with composition gradients. The nonlinear simulations immediately extended the mixed region, roughly equivalent to having used the Schwarzschild criterion at first. Because of fluctuations, this is evidently more nearly correct for the nonlinear case (Mocák et al. 2011, 2018). The Schwarzschild criterion is widely used in stellar codes instead of that of Ledoux, but without the theoretical justification that the fluctuations provide.

6. Composition and Boundaries

Boundaries, which figured prominently in Renzini’s critique, were not directly addressed in MLT. We now return to the issue: what is the nature of convective boundaries in our self-consistent simulations?

6.1. Dynamics at Stellar Boundaries

Boundaries of stellar convective regions are assumed to be adjacent to regions of convective stability (“radiative” regions assumed to have zero flow velocity). Thus convective flow must be joined to zero flow, which leads to the infinite accelerations and decelerations in MLT (the ends problem of Section 2) and to the singularity issue in Section 5.4.

The treatment of boundaries requires a consideration of dynamics not included in MLT: the boundary layer. The development of boundary layers is a prominent feature of our ILES (Figure 1). Because of fluctuations, convective flow at a boundary can only be zero on average, not always. This implies that the boundary moves and is a source of waves. Pure radial motion gives compression and sound waves. Non-radial motion is also nonzero, giving shear and gravity waves. At low Mach numbers, the g-waves dominate outside the boundary layers; only these are visible in Figure 1. Blue arrows indicate the boundary layers at top and bottom of the convective region. While evidence for waves is faint in this figure²⁷ below the bottom boundary layer, g-waves cause horizontal structures that are clearly visible above the top boundary layer.

Terrestrial experiments and numerical simulations show that convective and non-convective regions are separated by a boundary layer, which is required to join rotational ($\nabla \times \mathbf{v} \neq 0$) and potential ($\nabla \times \mathbf{v} = 0$) flow patterns (Landau & Lifshitz 1959, Section 44). Rotational flow is associated with mixing and potential flow is not. Such layers require large gradients to perform the joining of these very different flows, and thus the layers are often thin. These layers provide buoyancy braking to turn the flow, which implies negative buoyancy and thus a Brunt–Väisälä frequency that is real (Lighthill 1978, Section 4.1), so that these layers support waves (see Equation (10)). They are well mixed by the turbulent flow. In such layers, convective fluctuations must be coupled to wave production. Beyond these layers, in the radiative zone which may support a composition gradient, the Brunt–Väisälä frequency is also real, so internal waves are supported, and directly coupled to the boundary layer fluctuations. Because they can carry vorticity, g-waves can induce some mixing beyond the boundary layer; such mixing is energetically limited.

²⁶ The steady-state solution is actually unstable because of phase lag between damping and driving in ILES. This is an important part of the physics, which drives intermittency and waves.

²⁷ Such waves are robust and may be seen more clearly simply by using color maps chosen to emphasize them.

“One of the properties of the region of rotational turbulent flow is that the exchange of fluid between this region and the surrounding space can occur in only one direction. The fluid can enter this region from the region of potential flow, but can never leave it” (Landau & Lifshitz 1959, Section 34). Mixing, which increases entropy, gives the uni-directional nature of the exchange. Such entrainment of material from a radiative zone is a necessary aspect of convective boundaries, and one not included in MLT. This does not preclude receding convective regions, which could shed sub-regions of decaying turbulence that have been exposed to mixing; see also Holmes et al. (1996).

6.2. Distinct Boundary Regions

Based upon our 3D simulations, we construct a cartoon to clarify discussion of average properties; see Figure 3, which shows the upper boundary of a convection region (convective to the left, radiative to the right). There are five distinct regions, only two of which (1 and 5) are recognized in MLT:

1. Turbulent Convection. Inside r_1 , the superadiabatic excess is positive, as are the buoyant acceleration and the enthalpy flux. In this region, there is a balance between buoyant driving and turbulent dissipation (Section 5.4). This is the “convective” region of MLT (Böhm-Vitense 1958).
2. Braking. Between r_1 and r_2 the superadiabatic excess becomes negative, and the flow can turn and reverse direction. This is the “braking” region that is required dynamically. It has a negative enthalpy flux, is well mixed, and generates waves. This region does not exist in MLT, and is discussed in Arnett et al. (2015).
3. Shear. Between r_2 and r_3 is a boundary layer such as marked by arrows in Figure 1, and shown on an expanded scale in Figure 4. As horizontal components of the velocity grow at the expense of radial components (baryon conservation), the boundary layer develops high shear and is subject to shear instability (Drazin 2002).
4. Composition gradient. Between r_3 and r_4 is the region that can develop a composition gradient (see Figure 4), perhaps maintained at the margin of shear instability (Drazin 2002). This is not part of the original MLT (Böhm-Vitense 1958); it is the composition problem of Section 2. A “fix” must be added (e.g., “semi-convective” and/or “overshoot” regions). This has led to a search for algorithms to extend MLT, whose justification is that they are at least empirically desirable if not always self-consistent.
5. Radiative. Beyond r_4 is the “radiative” region of MLT. Unlike MLT, waves are automatically implied by flexing of the boundary layers (r_1 to r_4).

This crude cartoon is to be understood as a snapshot, which flexes and bends; its average properties are to be identified with stellar properties. The layers between r_1 and r_4 may be relatively thin in radial extent (see Figure 4). Regions 2 and 3 are not defined within MLT; they are part of the ends problem of Section 2. Region 4 is not defined within MLT because MLT assumes homogeneous composition (Böhm-Vitense 1958); in MLT, additional physics must be assumed concerning composition gradients to bridge this gap. This region is often treated as “semi-convective,” or partially mixed by “overshoot.” Mocák et al. (2011) used 2D simulations to examine

hydrodynamic mixing below shell convection zones; in this case, 2D is in qualitative agreement with 3D. Real overshoot involves regions 2, 3, and 4. Regions 2, 3, 4, and 5 all support waves and relate to the wind and waterline problem (Section 2). Any improvement over MLT will certainly affect regions 2, 3, and 4.

6.3. Composition Profile

To the extent that they are resolved, the 3D ILES simulations automatically produce dynamically self-consistent boundary physics for turbulent flow, with no additional assumptions required. In Paper II we show that our simulations with best spatial resolution do have small numerical error. Because the dynamic timescales for turbulent motion are usually so much faster than radiative diffusion timescales in stellar interiors, such boundary structure is set up rapidly. Figure 4 shows a composition profile of ^{16}O at the lower boundary of the turbulent oxygen burning shell.

The rms velocity profiles are shown for radial (red) and horizontal (blue) motion. The dominance of horizontal velocity (blue) for $r < 0.43 \times 10^9$ cm indicates g-waves. The boundary dynamics are those discussed in Arnett et al. (2015). The need for a turning flow requires that the radial velocity (red) approach zero faster than the horizontal velocities (blue), which have a peak near the boundary. There is a well-mixed region in which this braking and turning occur, and which is sub-adiabatic. Here the Brunt–Väisälä frequency is real; waves are generated by convective fluctuations and propagate from this region (see Section 4.5; Woodward et al. 2015, Figure 14).

The asymmetric behavior of convective boundaries, similar to that discussed in Gabriel et al. (2014) and Montalbán et al. (2013), can naturally arise in this braking region ($0.43 < r < 0.44 \times 10^9$ cm in Figure 4). It is a consequence of carefully joining turbulent flow to motion in a radiative region.

The sigmoid shape of the boundary is strikingly similar to that of the averaged mean flow of Garaud et al. (2017), obtained with DNS for a shear flow setup; see their Figure 3 (our use of the bottom boundary requires a flip in orientation). Arnett et al. (2015) showed that a turning plume would have such a shearing interface, even without differential rotation. The boundary conditions for differential rotation and convection seem to have a deep family resemblance.

Cristini et al. (2017, 2019) obtain a similar “sigmoid-like” profile for a carbon-burning shell. This shape from simulations has striking similarity to that inferred from asteroseismology (Arnett & Moravveji 2017) for the outer boundaries of convective cores of red giants. At first sight, this is puzzling; radiative diffusion has a very minor role in carbon and oxygen burning, but is important in red giants (Viallet et al. 2013). It suggests that the shape of the composition gradient may be insensitive to the effects of radiative diffusion. A clue appears in Figure 4, which shows a significant shear due to the horizontal velocities (blue curve), which may drive Kelvin–Helmholtz (KH) instabilities (Arnett et al. 2015). In the low Mach-number limit, this is a kinetic instability, driven just by the shape of the horizontal velocity in the radial direction (Drazin 2002, see Figure 8.3), and would be insensitive to radiative diffusion. See Section 3.3 in Woodward et al. (2015) for further discussion.

Our problem is more complex than the classical Rayleigh–Fjørtoft condition for KH instability (Drazin 2002), because our shear layer is bathed in pre-existing chaotic wave and

convective motions (due to fluctuations, Section 4). Rayleigh’s theorem states that a necessary condition for instability is that the radial velocity has an inflection point in radial coordinate (which the red line in Figure 4 suggests), so it is plausible that mixing occurs at the shearing boundary, as the numerical results indicate. Quantifying the rate of such mixing in stars deserves further study.

Consider a global perspective: as nuclear burning proceeds, the composition gradient steepens until KH instabilities induce some mixing to flatten it again. The gradient in velocity profile evolves toward neutral stability and lies near the composition profile that it sculpts, as shown in Figure 4. The finest resolution simulation seems to be approaching an asymptotic value; more evidence for this may be found in Paper II (Arnett et al. 2019). This asymptote is approached quickly, on a local timescale for turbulence.

An increase in entropy inside the convective zone tends to increase the size of the turbulent region. However, the effect of this increase may be sensitively dependent upon the gradients of thermal and compositional entropy in the boundary regions, as well as the turbulent velocity. A decrease in entropy gives a tendency to shed turbulent layers, which dissipate when no longer driven (Arnett et al. 2009). Again there may be a sensitive dependence upon the gradients of thermal and compositional entropy in the boundary regions, as well as the turbulent velocity. This is essentially the Richardson criterion for stability for a layered system (Turner 1973, Section 10.2.3).

7. Conclusion

We have (1) performed 3D turbulent ILES (Grinstein et al. 2007) of the classical Böhm-Vitense problem of stellar convection (Böhm-Vitense 1958), which have no other restrictions than zoning for this problem; (2) applied RA to these numerical results; and (3) developed several analytic approximations (321D) to illustrate the physics involved. We have systematically re-examined some unphysical aspects of MLT and of boundary physics in 1D stellar evolution, which were summarized in Renzini (1987).

We find that narrow boundary layers form to enclose the turbulent region, pulses of TKE are not significantly damped in 30 turnover times, and are associated with a few dominant rolls for weakly stratified convection, and although a Kolmogorov-like velocity spectrum forms, anisotropy is sufficient to give intermittency (Warhaft 2002).

It is not feasible in general to simulate stellar evolution in 3D at present, so that physically accurate approximations for longer times need to be developed. ILES work such as this, and the various simpler mathematical models we discuss, provide a foundation for refining and correcting such stellar evolution algorithms. While the ILES methods may be able to describe an explosion, for example, they become too expensive to deal with much of the previous, slower evolution that sets up the explosion.

The RA-ILES combination is “exact” to the word length of the computer used, unlike the RANS which are not closed (Tritton 1998). This advantage is a consequence of the sub-grid behavior of ILES, which mimics a Kolmogorov turbulent cascade, allowing both stellar size scales and turbulent scales to be described.

The evolution of the TKE is chaotic, involving a few dominant modes (unstable 3D rolls, Lorenz 1963). Driving and

damping of turbulent convection are out of phase; this makes interpretation of time aspects of numerical convergence a challenge, but provides insights into the dynamics of turbulence and stellar variability. These pulses of TKE are not an artifact of unphysical initial conditions. Stellar convection can quickly attain a dynamic steady state, with chaotic fluctuations.

The ILES simulations automatically provide a self-consistent structure at boundaries, including profiles of composition and velocity, structure of the deceleration region, and basis for study of wave generation. ILES allows us to describe a turbulent boundary layer, which uses a shear instability to sculpt a composition profile similar to that already inferred from asteroseismology (Arnett & Moravveji 2017). Entrainment of stable matter occurs at these dynamic boundary layers (Meakin & Arnett 2007b), at a rate dependent upon the particular stellar conditions. The process of turning the flow at the boundary also ensures that waves are generated, connecting the convective motion to the wave generation.

In Paper II (Arnett et al. 2019) we quantify the resolution errors due to cell size, and predict the turbulent dissipation length (the “mixing length”) from the simulations. We examine the unexplored case of strong stratification, in which the mixing length approaches an asymptotic limit close to that independently favored by the stellar evolution community.

We thank Prof. Alvio Renzini for thoughtful comments on the manuscript. We thank the Theoretical Astrophysics Program (TAP) at the University of Arizona and Steward Observatory for support.

S.W.C. acknowledges federal funding from the Australian Research Council through the Future Fellowship grant entitled “Where Are the Convective Boundaries in Stars?” (FT160100046). This work was supported in part by resources provided by the Pawsey Supercomputing Centre (Petascale Pioneers Program), with funding from the Australian Government and the Government of Western Australia, and by computational resources provided by the Australian Government through NCI via the National Computational Merit Allocation Scheme (project ew6).

This work used the Extreme Science and Engineering Discovery Environment (XSEDE), which is supported by National Science Foundation grant number OCI-1053575. Some computations in our work made use of ORNL/Kraken and TACC/Stampede.

A.C. acknowledges partial support from NASA Grant NNX16AB25G. A.C. acknowledges the use of resources from the National Energy Research Scientific Computing Center (NERSC), which is supported by the Office of Science of the U.S. Department of Energy under contract no. DEAC0205CH11231.

The authors acknowledge support from EUFP7ERC2012St Grant 306901. R.H. acknowledges support from the World Premier International Research Centre Initiative (WPI Initiative), MEXT, Japan. This article is based upon work from the ChETEC COST Action (CA16117), supported by COST (European Cooperation in Science and Technology). C.G., R.H., and C.M. thank ISSI, Bern, for their support on organizing meetings related to the content of this paper. C.G. acknowledges support from the Swiss National Science Foundation and from the Equal Opportunity Office of the University of Geneva.

This work used the DiRAC@Durham facility managed by the Institute for Computational Cosmology on behalf of the STFC DiRAC HPC Facility (www.dirac.ac.uk). The equipment was funded by BEIS capital funding via STFC capital grants ST/P002293/1 and ST/R002371/1, Durham University, and STFC operations grant ST/R000832/1. This work also used the DiRAC Data Centric system at Durham University, operated by the Institute for Computational Cosmology on behalf of the STFC DiRAC HPC Facility. This equipment was funded by BIS National E Infrastructure capital grant ST/K00042X/1, STFC capital grants ST/H008519/1 and ST/K00087X/1, STFC DiRAC Operations grant ST/K003267/1, and Durham University. DiRAC is part of the National E Infrastructure. We acknowledge PRACE for awarding us access to resource MareNostrum 4, based in Spain at Barcelona Supercomputing Center. The support of David Vicente and Janko Strassburg from Barcelona Supercomputing Center, Spain, to the technical work is gratefully acknowledged.

Appendix A Baryon Conservation

In an inertial frame,²⁸ with fluctuations, we have $\rho = \rho_0 + \rho'$, $\langle \rho \rangle = \rho_0$, $\langle \rho' \rangle = 0$ and $\mathbf{v} = \mathbf{v}_0 + \mathbf{v}'$, $\langle \mathbf{v} \rangle = \mathbf{v}_0$ and $\langle \mathbf{v}' \rangle = 0$. Thus

$$\langle \rho \mathbf{v} \rangle = \langle \rho_0 \mathbf{v}_0 \rangle + \langle \rho' \mathbf{v}' \rangle = 0 \quad (14)$$

requires the net mass flux from fluctuations to balance that of the base flow (e.g., Nordlund et al. 2009), giving a condition which conserves baryons.

The fluid-dynamic equations in an Eulerian coordinate system describe the flow of material through a fixed grid. In a Lagrangian system, a given amount of fluid is enclosed by a boundary that moves. The latter is awkward in more than 1D because of “grid tangling,” but is useful for stars, which approximate 1D spheres to some extent. Almost all stellar evolution codes are written on a 1D spherical Lagrangian grid in a “co-moving frame.” Let us examine how to map from a true 3D frame to a non-rotating 1D spherical frame (321D) and what this entails. Because information is lost, our result will be approximate to this extent.

Consider a spherical boundary (a “zone edge”) in a stellar evolutionary code. It is (1) spherical, and (2) except in special cases has zero net flow through it. In spherical coordinates, the net mass flow through radius $R(k)$ of the k th shell is

$$\frac{dm(k)}{dt} = R(k)^2 \int_0^{4\pi} \rho(R(k), \theta, \phi) [v(R(k), \theta, \phi) - U(k)] d\Omega, \quad (15)$$

where $U(k) = dR(k)/dt$ is the radial velocity of the boundary relative to the origin, and $\rho_0(R(k))$ is the average density at radius $R(k)$. We identify the angle average as $\langle \rho(r, \theta, \phi) \rangle = \rho_0(r)$.

To be co-moving, $\langle \rho \mathbf{v} \rangle / \langle \rho \rangle - U(k) = 0$, so we choose the difference $u - U(k)$ to be the radial component of fluctuation in velocity, v_r' . By this choice of coordinates, the average of the mass flux, over the whole solid angle is

$$\langle \rho_0 \mathbf{v}_0 \rangle = 0, \quad (16)$$

so that there is no net mass flux across the boundaries, in the base state of the stellar model, as we require for the co-moving spherical grid.

Now \mathbf{u}' is the 3D turbulent velocity fluctuation relative to the co-moving (stellar) grid of radius $R(k)$, and

$$\langle \rho' \mathbf{u}' \rangle = 0, \quad (17)$$

in this coordinate system, so fluctuations also cause no net transfer of baryonic mass, as designed. Thus \mathbf{u}' is the 3D velocity fluctuation relative to the center of momentum of the computational cell of the stellar model. For an inhomogeneous medium, correlations between velocity fluctuations and fluctuations of, for example, composition or enthalpy, will drive interesting currents (Arnett 1996, Section 4.6; Mocák et al. 2018) through the grid.

We have projected from 3D down to a static 1D spherical grid, and used a linear Galilean transform to the co-moving grid. Some information is lost (stars are not perfect spheres); an essential part of the 321D approximation is the projection of appropriate averaged quantities, which is guided by ILES and RA. Baryons are exactly conserved, but the complexity of non-spherical geometry is averaged over. Our coordinate system is now specified, and additional equations are required to define other fluxes through this grid.

Appendix B Momentum Conservation

We now transform the Navier–Stokes equation²⁹ to the co-moving frame. We have

$$\partial_t \rho \mathbf{v} + \nabla \cdot \rho \mathbf{v} \mathbf{v} = -\nabla P + \rho \mathbf{g} + \rho \nu \nabla^2 \mathbf{v}, \quad (18)$$

where $\rho \mathbf{v} \mathbf{v}$ is the Reynolds-stress tensor and ν the kinematic viscosity. One term, $\rho \mathbf{v} \mathbf{v}$, is nonlinear in \mathbf{v} , but this may be written in the co-moving frame by using mass conservation and taking a dot product with the velocity \mathbf{v} , which gives a kinetic energy equation,

$$d_t(\rho \mathbf{v} \cdot \mathbf{v} / 2) = -\mathbf{v} \cdot (\nabla P - \rho \mathbf{g} + \rho \nu \nabla^2 \mathbf{v}), \quad (19)$$

where we have compressed the left-hand side into a co-moving time derivative and taken the gravity vector to be appropriate for spherical geometry with $g' = 0$. We replace the viscous term with a Kolmogorov expression ϵ_K for its average (turbulent dissipation happens at small scales and we treat its average as local). Taking averages over a spherical shell (angles), and a few turnover times (overline), we have

$$d_t \overline{\langle \rho \mathbf{v} \cdot \mathbf{v} / 2 \rangle} = \overline{\langle -\mathbf{v} \cdot \nabla P - \rho \mathbf{v} \mathbf{g} \rangle} - \rho \epsilon_K. \quad (20)$$

See Meakin & Arnett (2007b); Nordlund et al. (2009); Viallet et al. (2013). An interesting result of the simulations is that the numerical result for ϵ_K agrees quantitatively with Kolmogorov’s analytic result for weak stratification, without this being explicitly imposed on the ILES results (see Kolmogorov 1941; Arnett et al. 2009, Paper II).

Using Equation (14) and integrating over a spherical shell gives $\langle \rho \mathbf{u}' \cdot \mathbf{g} \rangle = 0$ in a co-moving (Lagrangian), 1D coordinate system. Hydrostatic “equilibrium” (momentum balance in the co-moving stellar radial coordinate) is $-dP_0/dR - \rho_0 g = \rho_0 dU/dt$, which may be subtracted from Equation (20). In a steady state, this

²⁸ See Chapter 1, Weinberg (1927).

²⁹ See, e.g., Equation (15.7) in Landau & Lifshitz (1959).

equation becomes

$$-\overline{\langle \mathbf{u}' \cdot \nabla P' \rangle} = \overline{\langle \rho \epsilon_K \rangle}. \quad (21)$$

Now we use the identity

$$\mathbf{u}' \cdot \nabla P' + P' \nabla \cdot \mathbf{u}' \equiv \nabla \cdot (P' \mathbf{u}'), \quad (22)$$

so, after using hydrostatic equilibrium and mass conservation, Equation (21) becomes

$$\overline{\langle \rho \epsilon_K \rangle} = \overline{\langle \rho' \mathbf{u}' \cdot \mathbf{g} \rangle} + \overline{\langle P' \nabla \cdot \mathbf{u}' \rangle} - \overline{\langle \nabla \cdot (P' \mathbf{u}') \rangle}. \quad (23)$$

The three terms on the rhs are “buoyancy power,” “pressure dilatation,” and divergence of “acoustic flux.” For weak stratification and small Mach number, the second and third terms of the rhs (the “pressure dilatation” and divergence of “acoustic power”) are nearly zero (the turbulent pressure is small). This is not true for strong stratification, for which all three terms may be important (Paper II).

MLT is formulated in the weak stratification limit; the TKE production is then best understood as due to the remaining “buoyancy power” term, which is directly related to the enthalpy flux (Arnett et al. 2009). Mass conservation used alone causes the buoyancy term to be canceled (e.g., Nordlund et al. 2009), but the combined constraint of hydrostatic equilibrium causes it to reappear (Arnett & Meakin 2011). The pressure dilatation term in Equation (4) will prove important for strong stratification (Paper II, Arnett et al. 2019).

ORCID iDs

W. David Arnett  <https://orcid.org/0000-0002-6114-6973>

References

- Acton, F. S. 1970, *Numerical Methods That Work*, Harper International Edition (New York: Harper & Row)
- Aerts, C., Chistensen-Dalsgaard, J., & Kurtz, D. W. 2010, *Asteroseismology* (Berlin: Springer)
- Anderson, J. D. 2005, *PhT*, **58**, 42
- Apsden, A., Nikipforakis, N., Dalziel, S., & Bell, J. B. 2008, *CAMCOS*, **3**, 103
- Arnett, D. 1996, *Supernovae and Nucleosynthesis* (Princeton, NJ: Princeton Univ. Press)
- Arnett, W. D. 1968, *Natur*, **219**, 1344
- Arnett, W. D., & Meakin, C. 2010, in *IAU Symp. 265, Chemical Abundances in the Universe: Connecting First Stars to Planet*, 265, ed. K Cunha, M. Spite, & B. Barbuy (Cambridge: Cambridge Univ. Press), 106
- Arnett, W. D., & Meakin, C. 2011, *ApJ*, **741**, 33
- Arnett, W. D., & Meakin, C. 2016, *RPPPh*, **79**, 2901
- Arnett, W. D., Meakin, C., & Young, P. A. 2009, *ApJ*, **690**, 1715
- Arnett, W. D., Meakin, C. A., & Campbell, S. W. 2019, *ApJ*, submitted
- Arnett, W. D., Meakin, C. A., Viallet, M., et al. 2015, *ApJ*, **809**, 30
- Arnett, W. D., & Moravveji, E. 2017, *ApJ*, **836L**, 19
- Asplund, M., Nordlund, A., Trampedach, R., & Stein, R. F. 1999, *A&A*, **346**, L17
- Atroshchenko, I. N., & Gadun, A. S. 1994, *A&A*, **291**, 635
- Böhm-Vitense, E. 1958, *ZA*, **46**, 108
- Brown, B., Vasil, G., & Zweibel, E. 2012, *ApJ*, **756**, 109
- Canuto, V. M. 2012a, *A&A*, **528**, A76
- Canuto, V. M. 2012b, *A&A*, **528**, A77
- Canuto, V. M. 2012c, *A&A*, **528**, A78
- Canuto, V. M. 2012d, *A&A*, **528**, A79
- Canuto, V. M. 2012e, *A&A*, **528**, A80
- Canuto, V. M., Goldman, I., & Mazzitelli, I. 1996, *ApJ*, **473**, 550
- Canuto, V. M., & Mazzitelli, I. 1991, *ApJ*, **370**, 295
- Clayton, D. D. 1968, *Principles of Stellar Evolution and Nucleosynthesis* (New York: McGraw-Hill)
- Colella, P., & Woodward, P. 1984, *JCoPh*, **54**, 174
- Cristini, A., Hirschi, R., Arnett, W. D., et al. 2019, *MNRAS*, submitted
- Cristini, A., Meakin, C., Hirschi, R., et al. 2017, *MNRAS*, **471**, 279
- Davidson, P. A. 2001, *An Introduction to Magnetohydrodynamics* (Cambridge: Cambridge Univ. Press)
- Davidson, P. A. 2004, *Turbulence* (Oxford: Oxford Univ. Press)
- Dintrans, B., & Brandenburg, A. 2004, *A&A*, **421**, 775
- Drake, R. P. 2006, *High-Energy-Density Physics* (Berlin: Springer)
- Drazin, P. G. 2002, *Introduction to Hydrodynamic Stability* (Cambridge: Cambridge Univ. Press)
- Featherstone, N. A., & Hindman, B. W. 2016, *ApJ*, **830**, 15
- Frisch, U. 1995, *Turbulence* (Cambridge: Cambridge Univ. Press)
- Gabriel, M., & Belkacem, K. 2018, *A&A*, submitted
- Gabriel, M., Noels, A., Montalbán, J., & Miglio, A. 2014, *A&A*, **569**, A63
- Garaud, P., Gagnier, D., & Verhoeven, J. 2017, *ApJ*, **837**, 133
- Gough, D. O. 1967, *AJ*, **72**, 799
- Gough, D. O. 1969, *JATIS*, **26**, 448
- Gough, D. O. 1977, in *Proc. 38th Coll., Problems of Stellar Convection*, ed. E. A. Spiegel & J. P. Zahn (Berlin: Springer), 15
- Grinstein, Magolin, & Rider 2007, *Implicit Large Eddy Simulations* (Cambridge: Cambridge Univ. Press)
- Grossman, S. A., Narayan, R., & Arnett, D. 1993, *ApJ*, **407**, 284
- Hansen, C. J., Kawaler, S., & Trimble 2004, *Stellar Interiors: Physical Principles, Structure, and Evolution* (2nd ed.; New York: Springer)
- Haugen, N. E. L., & Brandenburg, A. 2004, *PhRvE*, **70**, 6405
- Haugen, N. E. L., & Brandenburg, A. 2006, *PhFI*, **18**, 075106
- Holmes, P., Lumley, J., & Berkooz, G. 1996, *Turbulence, Coherent Structures, Dynamical Systems and Symmetry* (Cambridge: Cambridge Univ. Press)
- Jones, S., Andrassy, S., Davis, A., Woodward, P., & Herwig, F. 2017, *MNRAS*, **465**, 2991
- Kippenhahn, R., & Weigert, A. 1990, *Stellar Structure and Evolution* (Berlin: Springer)
- Kolmogorov, A. N. 1941, *DoSSR*, **30**, 299
- Kolmogorov, A. N. 1962, *JFM*, **13**, 82
- Kufuss, R. 1986, *A&A*, **160**, 116
- Landau, L. D., & Lifshitz, E. M. 1959, *Fluid Mechanics* (London: Pergamon)
- Leveque, R. J. 2002, *Finite Volume Methods for Hyperbolic Problems* (Cambridge, UK: Cambridge Univ. Press)
- Lighthill, J. 1978, *Waves in Fluids* (Cambridge, UK: Cambridge Univ. Press)
- Lorenz, E. N. 1963, *JATIS*, **20**, 130
- Maeder, A. 1999, *Physics, Formation and Evolution of Rotating Stars* (Berlin: Springer)
- Manneville, P. 2010, *Instabilities, Chaos, and Turbulence* (London: Imperial College Press)
- Meakin, C. A., & Arnett, W. D. 2007a, *ApJ*, **665**, 690
- Meakin, C. A., & Arnett, W. D. 2007b, *ApJ*, **667**, 448
- Miesch, M., Featherstone, N., Rempel, M., & Trampedach, R. 2012, *ApJ*, **757**, L8
- Mocák, M., Meakin, C., Arnett, D., & Campbell, S. 2018, *MNRAS*, **481**, 2918
- Mocák, M., Meakin, C., Müller, E., & Siess, L. 2011, *ApJ*, **743**, 55
- Mocák, M., Meakin, C., Viallet, M., & Arnett, D. 2014, *arXiv:1401.5176*
- Montalbán, J., Miglio, A., Noels, A., et al. 2013, *ApJ*, **766**, 118
- Nordlund, A., Stein, R., & Asplund, M. 2009, *LRSF*, **6**, 2
- Orvendahl, R., Calkins, M., Featherstone, N., & Hindman, B. 2018, *ApJ*, submitted
- Parker, E. N. 1979, *Cosmic Magnetic Fields* (Oxford: Clarendon)
- Pope, S. B. 2000, *Turbulent Flows* (Cambridge, GB: Cambridge Univ. Press)
- Porter, D. H., & Woodward, P. R. 2000, *ApJS*, **127**, 159
- Prandtl, L. 1925, *ZaMM*, **5**, 136
- Renzini, A. 1987, *A&A*, **188**, 49
- Schindler, J.-T., Green, E. M., & Arnett, W. D. 2015, *ApJ*, **806**, 178
- Spiegel, E. A. 1971, *ARA&A*, **9**, 323
- Spiegel, E. A. 1972, *ARA&A*, **10**, 261
- Sytine, I. V., Porter, D. H., Woodward, P. R., Hodson, S. W., & Winkler, K.-H. 2000, *JCoPh*, **158**, 225
- Tennekes, H., & Lumley, J. L. 1972, *A First Course in Turbulence* (Cambridge MA: MIT Press)
- Tritton, D. J. 1998, *Physical Fluid Dynamics* (2nd ed.; Oxford UK: Oxford Univ. Press)
- Turner, J. S. 1973, *Buoyancy Effects in Fluids* (Cambridge, UK: Cambridge Univ. Press)
- Tzeferacos, P., Rigby, A., Bott, A. F. A., et al. 2018, *NatCo*, **9**, 591
- Unno, W. 1967, *PASJ*, **19**, 140
- Unno, W., Osaki, Y., Ando, H., Saio, H., & Shibahashi, H. 1989, *Nonradial Oscillations of Stars* (2nd ed.; Tokyo: Univ. of Tokyo)

- Verhoeven, J., Wiesehöfer, T., & Stellmach, S. 2015, [ApJ](#), 805, 62
- Viallet, M., Baraffe, I., & Walder, R. 2011, [A&A](#), 531, 86
- Viallet, M., Meakin, C., Arnett, D., & Mocák, M. 2013, [ApJ](#), 769, 1
- von Neumann, J., & Richtmeyer, R. D. 1950, [JAP](#), 21, 232
- Warhaft, Z. 2002, [PNAS](#), 99, 2481
- Weinberg, S. 1927, *Gravitation and Cosmology* (New York: J. Wiley & Sons)
- Whittaker, E. T., & Watson, G. N. 1927, *A Course of Modern Analysis* (Cambridge: Cambridge Univ. Press)
- Woodward, P. R. 2007, in *Implicit Large Eddy Simulation*, ed. F. F. Grinstein, L. G. Margolin, & W. J. Rider (Cambridge: Cambridge Univ. Press), 130
- Woodward, P. R., Herwig, F., & Lin, P.-H. 2015, [ApJ](#), 798, 49
- Xiong, D.-R. 1986, [A&A](#), 167, 239